

The *R*-Process Alliance: Abundance Universality among Some Elements at and between the First and Second *R*-Process Peaks*

IAN U. ROEDERER,^{1,2} JOHN J. COWAN,³ MARCO PIGNATARI,^{4,5,6,2} TIMOTHY C. BEERS,^{7,2} ELIZABETH A. DEN HARTOG,⁸
RANA EZZEDDINE,^{9,2} ANNA FREBEL,^{10,2} TERESE T. HANSEN,¹¹ ERIKA M. HOLMBECK,^{12,2} MATTHEW R. MUMPOWER,^{13,14,2}
VINICIUS M. PLACCO,¹⁵ CHARLI M. SAKARI,¹⁶ REBECCA SURMAN,^{17,2} AND NICOLE VASSH¹⁸

¹*Department of Astronomy, University of Michigan, 1085 S. University Ave., Ann Arbor, MI 48109, USA*

²*Joint Institute for Nuclear Astrophysics – Center for the Evolution of the Elements (JINA-CEE), USA*

³*Homer L. Dodge Department of Physics and Astronomy, University of Oklahoma, Norman, OK 73019, USA*

⁴*Konkoly Observatory, Research Centre for Astronomy and Earth Sciences, Eötvös Loránd Research Network (ELKH), MTA Centre of Excellence, Konkoly Thege Miklós út 15-17, H-1121 Budapest, Hungary*

⁵*E.A. Milne Centre for Astrophysics, Dept of Physics & Mathematics, University of Hull, HU6 7RX, United Kingdom*

⁶*NuGrid Collaboration, <http://nugridstars.org>*

⁷*Department of Physics and Astronomy, University of Notre Dame, Notre Dame, IN 46556, USA*

⁸*Department of Physics, University of Wisconsin-Madison, Madison, WI 53706, USA*

⁹*Department of Astronomy, University of Florida, Bryant Space Science Center, Gainesville, FL 32611, USA*

¹⁰*Department of Physics and Kavli Institute for Astrophysics and Space Research, Massachusetts Institute of Technology, Cambridge, MA 02139, USA*

¹¹*Department of Astronomy, Stockholm University, SE-106 91 Stockholm, Sweden*

¹²*Carnegie Observatories, Pasadena, CA 91101, USA*

¹³*Theoretical Division, Los Alamos National Laboratory, Los Alamos, New Mexico 87545, USA*

¹⁴*Center for Theoretical Astrophysics, Los Alamos National Laboratory, Los Alamos, New Mexico 87545, USA*

¹⁵*NSF's NOIRLab, Tucson, AZ 85719, USA*

¹⁶*Department of Physics and Astronomy, San Francisco State University, San Francisco, CA 94132, USA*

¹⁷*Department of Physics, University of Notre Dame, Notre Dame, IN 46556, USA*

¹⁸*TRIUMF, Vancouver, BC V6T 2A3, Canada*

(Accepted for publication in the *Astrophysical Journal* (ApJ 936, 84 (2022)))

ABSTRACT

We present new observational benchmarks of rapid neutron-capture process (*r*-process) nucleosynthesis for elements at and between the first ($A \sim 80$) and second ($A \sim 130$) peaks. Our analysis is based on archival ultraviolet and optical spectroscopy of eight metal-poor stars with Se ($Z = 34$) or Te ($Z = 52$) detections, whose *r*-process enhancement varies by more than a factor of 30 ($-0.22 \leq [\text{Eu}/\text{Fe}] \leq +1.32$). We calculate ratios among the abundances of Se, Sr through Mo ($38 \leq Z \leq 42$), and Te. These benchmarks may offer a new empirical alternative to the predicted solar system *r*-process residual pattern. The Te abundances in these stars correlate more closely with the lighter *r*-process elements than the heavier ones, contradicting and superseding previous findings. The small star-to-star dispersion among the abundances of Se, Sr, Y, Zr, Nb, Mo, and Te (≤ 0.13 dex, or 26%) matches that observed among the abundances of the lanthanides and third *r*-process-peak elements. The concept of *r*-process universality that is recognized among the lanthanide and third-peak elements in *r*-process-enhanced stars may also apply to Se, Sr, Y, Zr, Nb, Mo, and Te, provided the overall abundances of the lighter *r*-process elements are scaled independently of the heavier ones. The abundance behavior of the elements Ru through Sn ($44 \leq Z \leq 50$) requires further study. Our results suggest that at least one relatively common source in the early Universe produced a consistent abundance pattern among some elements spanning the first and second *r*-process peaks.

Email: iur@umich.edu

* Based on archival observations made with the NASA/ESA Hubble Space Telescope (program GO-7348, program GO-8342, program GO-9455, program GO-14161, and program GO-14672) and observations collected from the Keck Observatory Archive (program U25H).

Keywords: Nucleosynthesis (1131); R-process (1324); Stellar abundances (1577); Ultraviolet astronomy (1736);

1. INTRODUCTION

The rapid neutron-capture process, or r -process, produced heavy elements observed in the earliest generations of stars and about half of the heavy elements found in the solar system. A common view from theory is that compact binary mergers are a viable site of r -process nucleosynthesis (e.g., Rosswog et al. 2014; Grossman et al. 2014; Thielemann et al. 2017; Wehmeyer et al. 2019; Fernández et al. 2020; Farouqi et al. 2022). Rare kinds of supernovae may also be viable sites to contribute at least some r -process elements (e.g., Winteler et al. 2012; Nishimura et al. 2015; Siegel et al. 2019; Fischer et al. 2020; Yong et al. 2021), although normal core-collapse supernovae are not (e.g., Fischer et al. 2010; Roberts et al. 2010; Arcones & Thielemann 2013). Recent observations generally do not contradict the theoretical view. The kilonova emission observed following the merger of two neutron stars detected in gravitational waves appears to have been powered by the radioactive decay of a few $10^{-2} M_{\odot}$ of freshly produced r -process elements (e.g., Drout et al. 2017; Pian et al. 2017; Tanvir et al. 2017). The concentration of the short-lived radioactive r -process isotope ^{244}Pu in deep-sea sediments is consistent with a rare r -process source with high yields, such as neutron star mergers (Hotokezaka et al. 2015; Wallner et al. 2015, 2021). A small fraction ($\approx 10\%$) of the lowest-mass dwarf galaxies around the Milky Way exhibit high levels of r -process enhancement among most of their stars (Ji et al. 2016; Roederer et al. 2016b; Hansen et al. 2017), while all other galaxies in this mass range are extremely deficient in r -process elements (e.g., Frebel et al. 2010; Ji et al. 2019). Collectively these observations suggest that source(s) of r -process elements are rare but prolific events. Nevertheless, multiple sites may be required (e.g., Côté et al. 2019; Skúladóttir & Salvadori 2020).

The detailed element-by-element composition of r -process-enriched ejecta can be a powerful tool to distinguish among these candidates. Kilonova spectra offer, at best, limited prospects for measuring the detailed composition of ejected r -process material (Zhu et al. 2018; Watson et al. 2019; Wu et al. 2019). Uncertainties in calculating the atomic (Kasen et al. 2013; Fontes et al. 2020) and nuclear (Barnes et al. 2021; Zhu et al. 2021) data needed to interpret kilonova spectra are large. Old stars, on the other hand, retain heavy-element signatures dominated by individual r -process events. For example, 63 metals, including 42 r -process elements, have been detected in the metal-poor star HD 222925 (Roederer et al. 2018, 2022), which presents the most complete chemical inventory known for any object beyond the solar system.

These detailed chemical-abundance patterns provide a key link between stellar and nuclear astrophysics. Closed neutron shells relevant to the r -process occur in nuclei with neutron numbers $N = 50, 82, \text{ and } 126$. Their neutron-capture cross sections are reduced relative to neighboring nuclei, so they produce peaks in the abundance distribution. These peaks, at mass numbers $A \sim 80, 130, \text{ and } 195$, are sensitive probes of the physics of the r -process (e.g., Kratz et al. 1993; Dillmann et al. 2003; Panov et al. 2008; Eichler et al. 2015; Shibagaki et al. 2016; Reiter et al. 2020).

Many r -process-enhanced stars exhibit a consistent relative abundance pattern among the heavier r -process elements, here defined to be those with $56 \leq Z \leq 79$, including the lanthanide and third-peak elements. This pattern is a close match to the predicted solar system r -process residual pattern. This agreement implies that a robust r -process operates across the history of the Galaxy, a concept sometimes referred to as the “universality” of the r -process. Discussion of this phenomenon has appeared in Westin et al. (2000) and many reviews over the years, including those by Sneden et al. (2008), Frebel (2018), and Cowan et al. (2021).

The universal abundance pattern observed among the heavier r -process elements does not extend uninterrupted to the abundances of the lighter r -process elements. Many studies have shown that the abundances of lighter r -process elements, here defined to be those with $34 \leq Z < 56$, including the first- and second-peak elements, are less correlated with the abundances of heavier r -process elements (e.g., Wasserburg et al. 1996; McWilliam 1998; Johnson & Bolte 2002; Travaglio et al. 2004; François et al. 2007; Qian & Wasserburg 2008; Hansen et al. 2012). Studies of the similarities of the abundance ratios among strontium (Sr, $Z = 38$), yttrium (Y, $Z = 39$), zirconium (Zr, $Z = 40$), and other lighter r -process elements exist (e.g., Aoki et al. 2005; Ivans et al. 2006; Hansen & Primas 2011; Hansen et al. 2014; Wu et al. 2015; Aoki et al. 2017; Cain et al. 2018; Roederer et al. 2018; Spite et al. 2018), but generally they have not reported an analogous detection of universality among the abundances of the lighter r -process elements.

Theory predicts that many nucleosynthesis processes, in addition to the r -process, could potentially contribute to the abundances of these lighter r -process elements in the early Galaxy. These processes include the slow neutron-capture process (s -process) in fast rotating massive stars (e.g., Pignatari et al. 2008, 2010; Cescutti et al. 2013; Choplin et al. 2018; Limongi & Chieffi 2018), the intermediate neutron-capture process (i -process) (e.g., Roederer et al. 2016a; Banerjee et al. 2018; Clarkson et al. 2018), and proton-rich neutrino-driven wind com-

ponents from core-collapse supernovae (e.g., Fröhlich et al. 2006; Arcones & Montes 2011; Wanajo et al. 2018). The occurrence frequencies and the relative importance of these different stellar processes are matter of debate.

Here we contribute to this debate by exploring the star-to-star dispersion among the abundances of 12 lighter r -process elements. Our analysis begins with selenium (Se, $Z = 34$), the lightest element with a substantial r -process contribution (Roederer et al. 2022), and concludes at tellurium (Te, $Z = 52$), the heaviest element detectable with a mass less than barium (Ba, $Z = 56$) and the lanthanides. We introduce our stellar sample and present the abundances from the literature in Section 2. We analyze these abundances collectively for the first time in Section 3. We discuss the implications of our results in Section 4, and we summarize our conclusions in Section 5. We also present a minor update of abundances derived from ultraviolet (UV) spectra, motivated mainly by recent advances in the availability of atomic data, in Appendices A–C.

2. DATA

Elements at the three r -process peaks are readily detectable in UV spectra ($\lambda < 3100 \text{ \AA}$) collected using spectrographs on the Hubble Space Telescope. These elements include Se at the first peak (e.g., Roederer 2012; Roederer & Lawler 2012; Roederer et al. 2014b; Peterson et al. 2020); Te at the second peak (e.g., Roederer et al. 2012a,b, 2016a, 2022); and osmium (Os, $Z = 76$), iridium (Ir, $Z = 77$), and platinum (Pt, $Z = 78$) at the third peak (e.g., Cowan et al. 1996, 2005; Sneden et al. 1998; Den Hartog et al. 2005; Barbuy et al. 2011). Se and Te are more difficult to detect than Os, Ir, or Pt, because the Se I and Te I lines are found at shorter UV wavelengths ($2000 < \lambda < 2400 \text{ \AA}$) where longer exposure times are required to acquire sufficient signal-to-noise ratios. In practice, these observations are limited to only very bright stars with GALEX $NUV \lesssim 13.5$, or Johnson $V \lesssim 9$ for stars with effective temperature $> 5500 \text{ K}$.

Our sample includes all metal-poor stars with a Se or Te detection reported in the literature, and whose lanthanide elements exhibit abundance ratios dominated by the r -process; i.e., conform to the solar system r -process residual pattern. Only eight stars meet these criteria. A summary of their names, metallicities ($[\text{Fe}/\text{H}]$), abundance ratios of elements at the three r -process peaks ($[\text{Se}/\text{Fe}]$, $[\text{Te}/\text{Fe}]$, and $[\text{Pt}/\text{Fe}]$), and regions between the peaks ($[\text{Zr}/\text{Fe}]$ and $[\text{Eu}/\text{Fe}]$) are listed in Table 1. A complete list of the adopted abundances, including the adopted solar abundances, is presented in Appendix D. These eight stars span a range of metallicities and r -process abundance ratios: ≈ 1.1 dex in $[\text{Fe}/\text{H}]$, ≈ 0.7 dex in $[\text{Zr}/\text{Fe}]$, and ≈ 1.5 dex in $[\text{Eu}/\text{Fe}]$. The sample includes two highly r -process-enhanced stars ($[\text{Eu}/\text{Fe}] > +0.7$, as defined by Holmbeck et al. 2020), four moderately r -process-enhanced stars ($+0.3 < [\text{Eu}/\text{Fe}] \leq +0.7$),

and two stars with subsolar $[\text{Eu}/\text{Fe}]$ ratios. One star, HD 140283, satisfies the classification criteria proposed by Frebel (2018) for the “weak” or “limited” r -process: $[\text{Eu}/\text{Fe}] < +0.3$, $[\text{Sr}/\text{Ba}] > +0.5$, and $[\text{Sr}/\text{Eu}] > 0.0$. The complete abundance patterns for these stars are available from the references listed in Table 1. We update the abundances to a common $\log(gf)$ scale, with references given in Roederer et al. (2022).

Appendix D also lists the stellar parameters for the stars in our sample. They span a range of evolutionary states, from the main sequence to the red horizontal branch. Previous studies (Aoki et al. 2010; Preston et al. 2006; Roederer et al. 2014a) have established that the r -process abundance pattern is recognizable in stars of all such evolutionary states and is not impacted by the internal changes that lead to stellar evolution.

The stars in our sample were originally selected for observations with the Space Telescope Imaging Spectrograph (STIS; Kimble et al. 1998; Woodgate et al. 1998) for heterogeneous reasons. HD 222925 and BD +17°3248 were selected on the basis of their high $[\text{Eu}/\text{Fe}]$ ratios (europium, $Z = 63$). HD 108317 and HD 128279 were selected because they share similar stellar parameters but exhibit a moderate contrast in their $[\text{Eu}/\text{Fe}]$ ratios. HD 19445, HD 84937, HD 140283, and HD 160617 were selected without regard to their heavy-element abundances. These stars do not represent a comprehensive sample of heavy-element abundance patterns observed in metal-poor stars. As we show, however, they exhibit a high degree of similarity in abundances of elements that played no role in their original selection for observations.

3. RESULTS

3.1. Abundance Behaviors

The $[\text{X}/\text{Fe}]$ ratios (for $\text{X} = \text{Se}, \text{Zr}, \text{Te}, \text{Eu},$ and Pt) listed in Table 1 are correlated. The Pearson correlation coefficients are $r > 0.65$ for each of these relationship pairs, indicating a high degree of correlation. Figure 1 shows the very high degree of correlation ($r = 0.91$) between the $[\text{Zr}/\text{Fe}]$ and $[\text{Eu}/\text{Fe}]$ ratios. The slope of the correlation is 0.45, considerably less than 1.0. In the analysis that follows, we account for this fact by scaling the abundances of heavier r -process elements to Eu and scaling the abundances of lighter r -process elements to Zr. Zr and Eu are chosen because they are detected in all eight stars, are typically measured from multiple unsaturated lines of the dominant ionization state, and their atomic transition probabilities are well known and do not dominate the uncertainty budget.

Figure 1 also demonstrates that the stars in our sample provide a reasonable representation of the $[\text{Zr}/\text{Fe}]$ and $[\text{Eu}/\text{Fe}]$ ratios found in metal-poor stars. The small dots in Figure 1 are drawn from literature samples of metal-poor field stars that are not enhanced in carbon or s -process elements. Stars enhanced in r -process elements are overrepresented in this comparison sample,

Table 1. Stellar Sample, Sorted by Decreasing [Eu/Fe] Ratios

Star	[Fe/H]	[Se/Fe]	[Zr/Fe]	[Te/Fe]	[Eu/Fe]	[Pt/Fe]	References
HD 222925	-1.46 ± 0.10	$+0.74 \pm 0.22$	$+0.62 \pm 0.08$	$+0.91 \pm 0.14$	$+1.32 \pm 0.08$	$+1.29 \pm 0.10$	1
BD +17°3248	-2.10 ± 0.20	...	$+0.35 \pm 0.14$	$+0.34 \pm 0.30$	$+0.90 \pm 0.04$	$+1.01 \pm 0.07$	2, 3, 4, 5
HD 108317	-2.37 ± 0.14	$+0.47 \pm 0.42$	$+0.24 \pm 0.20$	$+0.41 \pm 0.30$	$+0.48 \pm 0.18$	$+0.51 \pm 0.19$	6, 7, 8
HD 160617	-1.77 ± 0.29	$+0.14 \pm 0.21$	$+0.24 \pm 0.30$	$+0.41 \pm 0.32$	$+0.44 \pm 0.29$	$+0.74 \pm 0.21$	9 ^a , 10
HD 84937	-2.25 ± 0.10	$+0.14 \pm 0.20$	$+0.31 \pm 0.10$	$+0.40 \pm 0.15$	$+0.38 \pm 0.15$	$< +0.53$	10, 11
HD 19445	-2.15 ± 0.10	$+0.37 \pm 0.23$	$+0.38 \pm 0.10$	$+0.62 \pm 0.15$	$+0.37 \pm 0.15$	$< +0.73$	10, 11
HD 128279	-2.46 ± 0.14	-0.31 ± 0.36	-0.12 ± 0.20	$+0.18 \pm 0.30$	-0.02 ± 0.18	$< +0.08$	6, 7, 8
HD 140283	-2.57 ± 0.10	$+0.37 \pm 0.20$	-0.07 ± 0.10	$< +0.59$	-0.22 ± 0.10	< -0.45	10, 11

References—1 = Roederer et al. (2022); 2 = Cowan et al. (2002); 3 = Sneden et al. (2009); 4 = Den Hartog et al. (2005); 5 = Appendix A; 6 = Roederer et al. (2012b); 7 = Roederer et al. (2014c); 8 = Appendix C; 9 = Roederer & Lawler (2012); 10 = Peterson et al. (2020); 11 = Appendix B.

NOTE—[X/Y] $\equiv \log_{10}(N_X/N_Y) - \log_{10}(N_X/N_Y)_\odot$

^aThe Ir abundance is considered an upper limit, following discussion in Ref. 7.

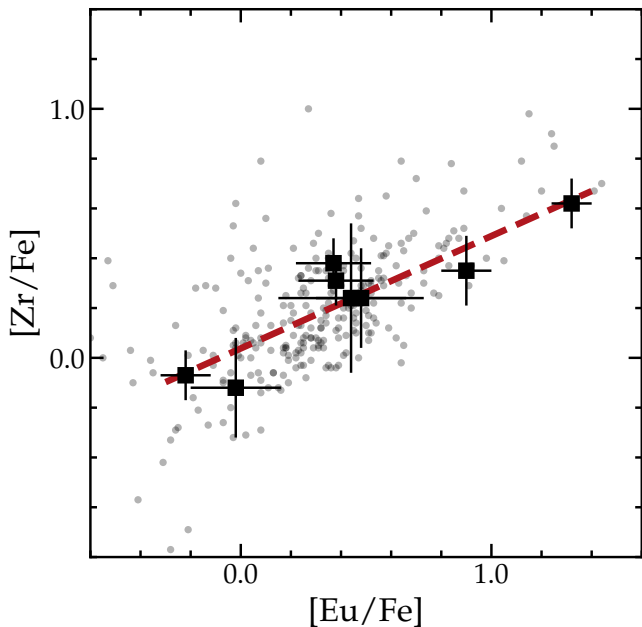


Figure 1. [Zr/Fe] versus [Eu/Fe] ratios in our sample (squares). The red dashed line marks a linear fit to these eight stars. A strong correlation with slope less than 1 is observed. The small gray circles mark stars drawn from the literature (Burris et al. 2000; Fulbright 2000; Johnson 2002; Honda et al. 2004; Barklem et al. 2005; François et al. 2007; Lai et al. 2008; Ishigaki et al. 2013; Roederer et al. 2014b), as found in JINAbase (Abolalima & Frebel 2018).

because it is easier to detect Zr and Eu when their abundances are enhanced. Nevertheless, despite the rela-

tively limited availability of stars with low levels of Zr and Eu, this comparison sample also exhibits a similar correlation between the [Zr/Fe] and [Eu/Fe] ratios.

Figure 2 illustrates the abundances of the stars in our sample. The left panels show the lighter r -process elements, $34 \leq Z \leq 52$, scaled to the Zr abundance in each star. The right panels show the heavier r -process elements, $56 \leq Z \leq 79$, scaled to the Eu abundance in each star. The right panels of Figure 2 illustrate the phenomenon commonly known as the universality of the r -process. The heavy elements in these stars exhibit minimal star-to-star abundance dispersion when scaled to account for the overall amount of r -process material in each star. We calculate the median absolute deviation (MAD) as a robust measure of the dispersion in each $\log \varepsilon(X/Eu)$ ratio (for $X = Ba$ to Au). These dispersions, shown in the bottom-right panel of Figure 2, are typically small. The abundances of most of the lanthanide elements are frequently derived from many unsaturated and unblended lines in high-quality optical spectra. The red line in the bottom panels of Figure 2 marks 0.13 dex (26%), which is the upper boundary to the dispersion among the lanthanide and third r -process-peak element ratios.

Our choice to scale the abundances of lighter elements separately reveals previously unrecognized abundance behavior. A small star-to-star dispersion is also observed among many elements in the left panels of Figure 2. The dispersions among the $\log \varepsilon(X/Zr)$ ratios (for $X = Se, Sr, Y, Nb, Mo,$ and Te) are all small, ≤ 0.13 dex (26%), as shown in the bottom-left panel of Figure 2. These values are also listed in Table 2, along with the standard errors (std. err.) and standard deviations (std. dev.). These dispersions are comparable to the disper-

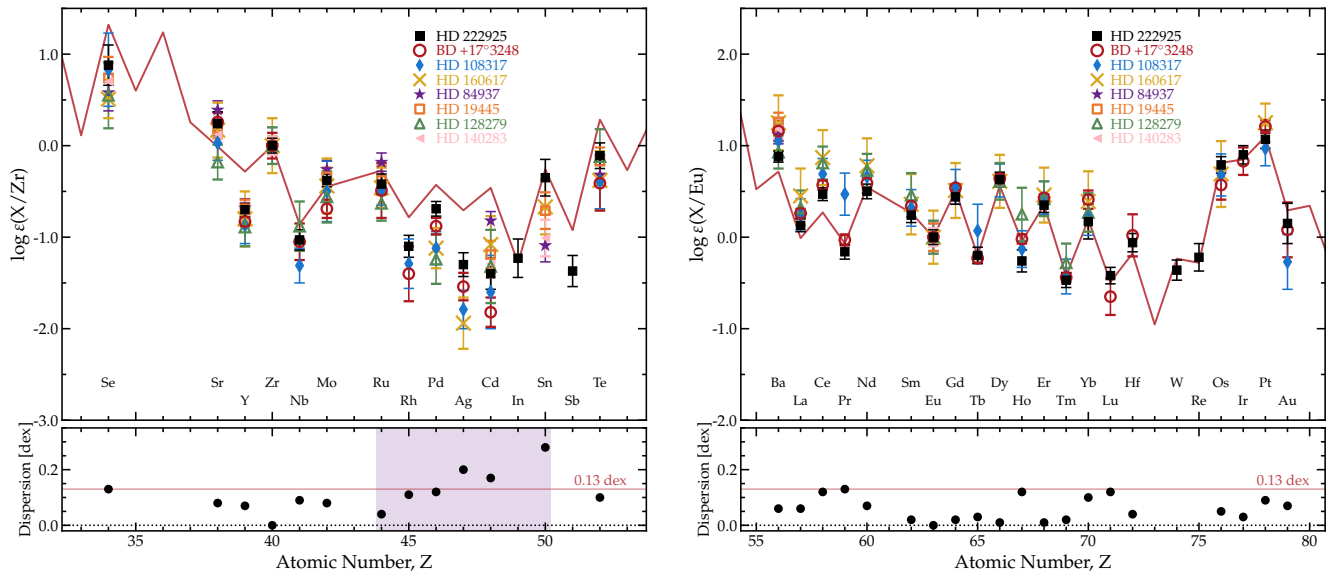


Figure 2. Left: Abundances of lighter r -process elements, scaled to the Zr abundance in each star. The legend is sorted by decreasing $[\text{Eu}/\text{Fe}]$ ratios (Table 1). Right: Abundances of heavier stable r -process elements, scaled to the Eu abundance in each star. The red line in each panel marks the scaled solar system r -process residuals (Prantzos et al. 2020). The vertical axes span 4.5 dex in both panels. The bottom panels illustrate the dispersions of the $\log \varepsilon(X/Zr)$ or $\log \varepsilon(X/Eu)$ abundance ratios. The dotted line in the bottom panels represents a dispersion of zero, and the red lines represent dispersions of 0.13 dex. The light purple box marks elements with conflicting abundance information, or that may receive a substantial contribution from mechanisms beyond the scope of the present study (Section 3.2), and they are not considered further here.

Table 2. Benchmark Abundance Ratios

X_1/X_2	$\log \varepsilon(X_1/X_2)$	std. err.	std. dev.	MAD
		[dex]	[dex]	[dex]
Se/Zr	0.70	0.10	0.13	0.13
Sr/Zr	0.20	0.06	0.16	0.08
Y/Zr	-0.73	0.06	0.08	0.07
Nb/Zr	-1.06	0.10	0.16	0.08
Mo/Zr	-0.42	0.06	0.13	0.06
Te/Zr	-0.23	0.08	0.12	0.10
Se/Te	0.93	0.13	0.16	0.05

NOTE— $\log \varepsilon(X_1/X_2) \equiv \log_{10}(N_{X_1}/N_{X_2})$

sions among the heavier r -process elements. Critically, each individual $\log \varepsilon(X/Zr)$ ratio (for $X = \text{Se}, \text{Sr}, \text{Y}, \text{Nb}, \text{Mo},$ and Te) in each star agrees to better than 2σ with the median calculated for the sample of eight stars. Therefore, we propose that the abundance ratios among Se, Sr, Y, Zr, Nb, Mo, and Te are also universal, at the precision of available observational data, provided that their abundances are scaled independently of the heavier elements.

Analysis of the abundance ratios found in a much larger sample of metal-poor stars supports this conclusion. Among the stars that are not classified as carbon enhanced, s -process rich, i -process rich, or $r + s$ in the JINAbase abundance database (Abohalima & Frebel 2018), the MAD of the $\log \varepsilon(\text{Sr}/\text{Zr})$, $\log \varepsilon(\text{Y}/\text{Zr})$, and $\log \varepsilon(\text{Mo}/\text{Zr})$ ratios are 0.14, 0.11, and 0.08 dex, respectively, based on samples of 294, 294, and 13 stars. Dispersions among the Sr, Y, Zr, and Mo abundance ratios for this larger sample are comparable to or smaller than our adopted 0.13 dex dispersion criterion. Less than 1.4% of the stars in this sample exhibit $\log \varepsilon(X/Zr)$ (for $X = \text{Sr}, \text{Y},$ or Mo) ratios that clearly deviate by more than 2σ from the median value of each ratio. We regard the consistency in these ratios as superb, considering the wide range of spectral quality and inhomogeneous abundance analyses reflected in the JINAbase sample. This test suggests that the ratios among Sr, Y, Zr, and Mo abundances are similarly consistent in most metal-poor stars.

3.2. Ruthenium through Tin

Figure 2 indicates that the elements ruthenium (Ru, $Z = 44$), rhodium (Rh, $Z = 45$), and palladium (Pd, $Z = 46$) also exhibit dispersions smaller than 0.13 dex in our sample. The elements silver (Ag, $Z = 47$), cadmium (Cd, $Z = 48$), and tin (Sn, $Z = 50$) exhibit dispersions larger than 0.13 dex in our sample. These elements are

highlighted by the purple shaded box in Figure 2. We now discuss these elements’ behavior in more detail.

Our Ru results, viewed in isolation, favor the opposite conclusion than that drawn by Aoki et al. (2017). That study, based on a sample of six stars, concluded that the Ru/Zr ratios exhibit significant star-to-star dispersion. On one hand, the $\log \varepsilon(\text{Ru/Zr})$ ratios of the stars in their sample agree to within 2σ , which we would not consider to be a significant dispersion. On the other hand, Aoki et al. also combined their sample with results from Sneden et al. (2003) (1 star) and Hansen et al. (2012, 2014) (12 giant stars with $[\text{Fe/H}] < -2.0$). Collectively, the three samples exhibit a range of $[\text{Ru/Zr}]$ ratios spanning ≈ 0.9 dex, a fact that supported their finding of a significant dispersion among the Ru/Zr abundance ratios. If we combine our sample with the Aoki et al. expanded sample, we calculate $\text{MAD} = 0.16$ dex, which we agree signals a significant dispersion in the Ru/Zr abundance ratios. A similar calculation for the $\log \varepsilon(\text{Sr/Zr})$, $\log \varepsilon(\text{Y/Zr})$, and $\log \varepsilon(\text{Mo/Zr})$ ratios in the Aoki et al. expanded sample plus ours yields MADs of 0.09, 0.06, and 0.09 dex. We thus confirm the results of Aoki et al. that there are no significant differences among the abundances of Sr, Y, Zr, and Mo. We conclude that the Ru/Zr ratios may exhibit significant dispersion, although our sample alone does not reveal such evidence. A homogeneously analyzed larger sample of stars may be necessary to definitively assess the abundance behavior of Ru.

The $\log \varepsilon(\text{X/Zr})$ ratios for $\text{X} = \text{Rh}, \text{Pd}, \text{Ag}, \text{Cd},$ and Sn exhibit a moderate amount of dispersion in our sample, $0.11 \leq \text{MAD} \leq 0.28$ dex. Vassh et al. (2020) have proposed that these elements could receive a substantial contribution from fission fragments in some stars. We explore the abundance behaviors of these elements separately (Roederer et al., in preparation), and so we do not discuss them further here.

3.3. Tellurium

Te isotopes occupy the mass region that could mark the transition between the “lighter” and “heavier” r -process elements, so we discuss the Te abundances further in this section. The Te abundances in our sample correlate more strongly with the lighter elements than the heavier ones, as shown in Figure 3. The MAD and standard deviation of the $\log \varepsilon(\text{Te/Zr})$ ratios are only 0.10 dex and 0.12 dex, while the MAD and standard deviation of the $\log \varepsilon(\text{Te/Eu})$ ratios are much larger, 0.23 dex and 0.28 dex. These differences in the dispersions cannot be due to differing observational uncertainties, because the median uncertainty in the Zr abundances, 0.10 dex, is actually larger than the median uncertainty in the Eu abundances, 0.06 dex. Te associates more naturally with the lighter r -process elements than the heavier ones in this sample of stars.

Roederer et al. (2012a) reported that Te abundances match the solar r -process residual pattern when scaled

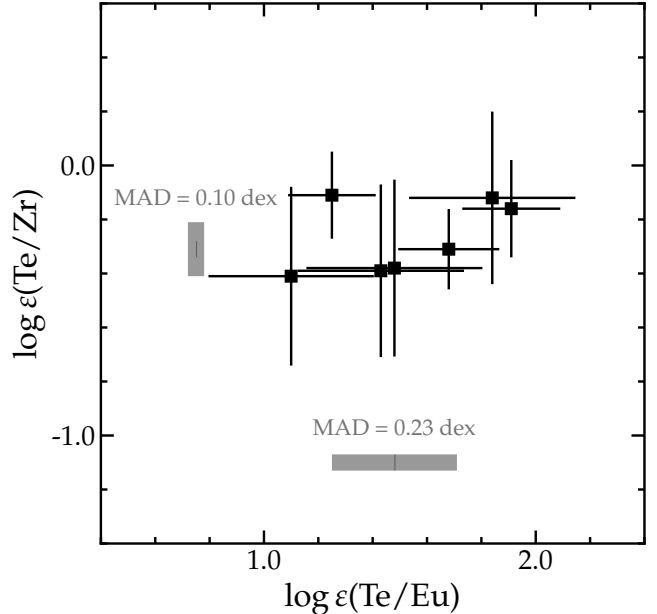


Figure 3. $\log \varepsilon(\text{Te/Zr})$ versus $\log \varepsilon(\text{Te/Eu})$ ratios in our sample (black squares). The shaded bars illustrate the median \pm MAD for each ratio. The MAD of the $\log \varepsilon(\text{Te/Zr})$ ratio is much smaller than that of the $\log \varepsilon(\text{Te/Eu})$ ratio.

to Eu. Our result supersedes that one. The mean $\log \varepsilon(\text{Te/Eu})$ ratio in this sample is 1.52 ± 0.09 ($\sigma = 0.28$ dex), whereas the solar system r -process residuals from Goriely (1999), Sneden et al. (2008), Bisterzo et al. (2011, 2014), and Prantzos et al. (2020) predict $\log \varepsilon(\text{Te/Eu})_{\odot,r} = 1.60, 1.64, 1.62,$ and 1.60 , respectively. The Te abundances in this particular sample of stars are low relative to the solar r -process residual pattern by only ≈ 0.1 dex, which is not significant.

We emphasize, however, that the Te abundances are more closely correlated with the lighter r -process elements, such as Zr, than the heavier r -process elements, such as Eu. We conclude that the transition from the lighter to the heavier r -process elements likely occurs between Te and Ba, around mass numbers $130 \lesssim A \lesssim 135$.

3.4. Observational Benchmarks

The weighted mean $\log \varepsilon(\text{X/Zr})$ ratios for the elements that do not exhibit significant star-to-star dispersion ($\text{X} = \text{Se}, \text{Sr}, \text{Y}, \text{Nb}, \text{Mo}, \text{Te}$) are listed in Table 2. Table 2 also lists the weighted mean $\log \varepsilon(\text{Se/Te})$ ratio as a measure of the relative heights of the first and second r -process peaks.

We compare a few of these key ratios with predictions for the solar system r -process residuals. The mean $\log \varepsilon(\text{Se/Zr})$ ratio is 0.70 ± 0.10 . The solar system r -process residuals from Goriely (1999), Sneden et al. (2008), Bisterzo et al. (2011, 2014), and Prantzos et al. (2020) predict $\log \varepsilon(\text{Se/Zr})_{\odot,r} = 1.12, 0.89, 1.22,$ and

1.33, respectively, which are higher by ≈ 0.2 – 0.6 dex than the ratios found in our sample of metal-poor stars. The mean $\log \varepsilon(\text{Te}/\text{Zr})$ ratio is -0.23 ± 0.08 . The solar system r -process residuals from the same four references predict $\log \varepsilon(\text{Te}/\text{Zr})_{\odot,r} = 0.12, 0.29, 0.03, \text{ and } 0.28$, respectively, which are higher by ≈ 0.3 – 0.5 dex than the ratios found in our sample of metal-poor stars. The mean $\log \varepsilon(\text{Se}/\text{Te})$ ratio is 0.93 ± 0.13 . This value is within the range of the solar system r -process residual predictions from the same four references, $\log \varepsilon(\text{Se}/\text{Te})_{\odot,r} = 1.00, 0.60, 1.19, \text{ and } 1.05$, respectively. The values listed in Table 2 offer empirical r -process abundance ratios that are independent of the solar abundances.

Our proposed application of the concept of universality (Section 3.1) does not require a match to the solar system r -process residual pattern, as in the case of the heavier r -process elements, because the r -process residual pattern for lighter elements may be compromised. Its derivation assumes that the solar system abundance pattern contains material from only the r -process, s -process, and proton-capture process (p -process). This key assumption is likely invalid (e.g., Travaglio et al. 2004; Bisterzo et al. 2017; Côté et al. 2018). Thus, the fair but imperfect agreement between the r -process residual pattern and the stellar Se, Sr, Y, Zr, Nb, Mo, and Te abundances does not contradict the operation of a robust r -process across cosmic time. If multiple r -process sources operate, their occurrence frequencies may have been different in the early Galaxy than they are in the Galactic disk (e.g., Côté et al. 2019). This scenario could offer one explanation for the differences between the solar system r -process residual pattern and the benchmark abundance pattern presented here.

3.5. Comparison with Other Classes of r -process-Enhanced Stars

In this section we search for differences between the lighter r -process-element abundance pattern found in our sample and that found in two other classes of stars. One class is the r -process-enhanced stars with the so-called actinide boost, characterized by high Th/Eu ratios, here defined to be $\log \varepsilon(\text{Th}/\text{Eu}) > -0.40$, relative to most other r -process-enhanced stars. This class includes 11 stars: CS 22953–003 (Roederer et al. 2014b), CS 30306–132 (Honda et al. 2004), CS 30315–029 (Siqueira Mello et al. 2014), CS 31078–018 (Lai et al. 2008), CS 31082–001 (Siqueira Mello et al. 2013), HD 6268 (Roederer et al. 2014b), HE 1219–0312 (Hayek et al. 2009), HE 2252–4225 (Mashonkina et al. 2014), HE 2327–5642 (Mashonkina et al. 2010), J0954+5246 (Holmbeck et al. 2018), and SMSS J2003–1142 (Yong et al. 2021). Abundances for Sr, Y, and Zr are reported for each star, but abundances for Nb and Mo are only available for one and six stars in this set, respectively. None of the $\log \varepsilon(\text{X}/\text{Zr})$ ratios (for X = Sr, Y, Nb, or Mo) in these stars differ by more than 2σ from the mean benchmark ratios.

The other class of stars is the so-called weak (or limited) r -process stars. It is exemplified by two stars examined by Honda et al. (2006, 2007), HD 88609 and HD 122563, which exhibit relatively low enhancements of the elements beyond the second r -process peak. Abundances of Sr, Y, Zr, Nb, and Mo are available for these two stars. None of the $\log \varepsilon(\text{X}/\text{Zr})$ ratios in these stars differs by more than 2σ from the mean benchmark ratios, with the exception of the $\log \varepsilon(\text{Nb}/\text{Zr})$ ratio in HD 88609, which is low by only $\approx 2.3\sigma$.

We conclude from these comparisons that neither class of stars exhibits significantly different abundance behavior among the elements from Sr through Mo. It would be worthwhile to perform similar comparisons for the Se and Te abundances, which, unfortunately, are not available at present for any of the stars in these classes.

3.6. The Impact of Potential Contamination

We assume that the abundance patterns in these stars reflect only r -process nucleosynthesis. Other processes could contribute to the heavy elements in these stars, in principle, as discussed in Section 1. We construct a toy model to test our assumption using the $\log \varepsilon(\text{Se}/\text{Zr})$ and $\log \varepsilon(\text{Te}/\text{Zr})$ ratios. We explore the consequences of s -process and i -process contamination from short-lived massive stars that could have enriched the gas from which the stars in our sample were formed. For now, we do not distinguish between a weak (or limited) r -process and a main r -process, and we defer this discussion to Section 4.

We adopt a set of s -process abundance ratios representative of the production in fast-rotating massive stars (e.g., Pignatari et al. 2008; Frischknecht et al. 2016; Choplin et al. 2018; Limongi & Chieffi 2018). We use a single-zone trajectory from a $25 M_{\odot}$ star with an initial metallicity of $Z = 10^{-4}$ ($[\text{Fe}/\text{H}] = -2.14$), calculated using the Geneva stellar evolution code GENEC (Hirschi et al. 2004). This model is representative of stars with s -process production during both core He-burning and shell C-burning (Nishimura et al. 2017). We perform these nucleosynthesis calculations using the post-processing network code PPN (Pignatari & Herwig 2012). We adopt the parametric approach used by Pignatari et al. (2013) to account for the possible range of s -process production, by varying the amount of primary ^{22}Ne destroyed to make neutrons via the $^{22}\text{Ne}(\alpha, n)^{25}\text{Mg}$ reaction. Nine sets of s -process ratios, ranging from $-0.74 \leq \log \varepsilon(\text{Se}/\text{Zr}) \leq 1.62$ and $-2.43 \leq \log \varepsilon(\text{Te}/\text{Zr}) \leq -0.96$, are considered.

One-dimensional massive star models incorporating i -process calculations exist, but they await verification by comprehensive hydrodynamics simulations that are able to resolve and capture the main properties of these types of events (e.g., Herwig et al. 2014; Woodward et al. 2015). Accordingly, we adopt a simplified set of i -process conditions that qualitatively capture the main properties of i -process abundance patterns with differ-

ent amounts of neutrons. We use the nucleosynthesis framework adopted in Bertoli et al. (2013) and Roederer et al. (2016a) for a metallicity of $[\text{Fe}/\text{H}] = -2.2$. Seven i -process neutron exposures are considered, producing abundance ratios that range from $-1.76 \leq \log \varepsilon(\text{Se}/\text{Zr}) \leq 1.67$ and $-1.35 \leq \log \varepsilon(\text{Te}/\text{Zr}) \leq 1.20$.

Finally, we adopt r -process abundance ratios from the observationally derived values presented in Table 2.

We calculate seven realizations of the $\log \varepsilon(\text{Se}/\text{Zr})$ and $\log \varepsilon(\text{Te}/\text{Zr})$ ratios in each simulation, matching the number of stars in our sample where each ratio is derived. We adjust the mean relative mix of material from the different neutron-capture processes. Each component of the input mixture is multiplied by a random number between 0 and 1 in each simulation to account for variability in the mixtures, although the overall mean relative mix is maintained in each simulation. We also inject observational uncertainties into each of these ratios. The mean (median) observational uncertainties in the Se and Te abundances are 0.26 dex (0.22 dex) and 0.24 dex (0.30 dex), respectively, so we apply a generously small 0.2 dex observational uncertainty to our resampled abundances. We then calculate the standard deviation of the seven resamples of each ratio. We repeat this process 10^4 times.

We conduct simulations with 95/5, 80/20, and 50/50 % mean mixes between the r -process ratios and each of the s -process and i -process ratios. We also conduct a simulation with equal mixes of all three sets of ratios. Fewer than 5% of these simulations in any given mixture exhibit equal or less dispersion than our sample, and the percentage is $< 2\%$ for the majority of these simulations. This unsurprising result indicates that the inclusion of material from other processes can only increase the dispersion in the observed abundance ratios.

Alternatively, contamination could bias the means of these ratios. We consider this possibility unlikely. The dominance of the r -process that contributed heavy elements to HD 222925, which has the most r -process material among stars in our sample ($[\text{Eu}/\text{Fe}] = +1.32$, $\log \varepsilon(\text{Eu}) = 0.38$), masks any contributions from other sources to HD 222925. However, this star exhibits statistically indistinguishable abundance ratios among Se, Sr through Mo, and Te when compared to stars with much lower levels of r -process enhancement ($-0.22 \leq [\text{Eu}/\text{Fe}] \leq +0.90$) or enrichment ($-2.27 \leq \log \varepsilon(\text{Eu}) \leq -0.68$). Any bias from contamination is smaller than 0.13 dex (26%), on average.

4. DISCUSSION

For the eight stars examined in this work, the abundances of the heavy r -process elements exhibit ratios constant to within a dispersion of 0.13 dex, roughly equivalent to observational precision. This uniformity persists despite the $[\text{Eu}/\text{Fe}]$ ratios changing by a factor of more than 30, a fact established by previous work (e.g., Spite et al. 2018). We demonstrate, using the same

stars, that the r -process abundance ratios among the elements Se, Sr, Y, Zr, Nb, Mo, and Te exhibit star-to-star dispersion comparable to that exhibited by the lanthanides and, when detected, the third-peak elements. We propose that, in this case, the universality of these lighter r -process elements at and between the first and second r -process peaks mirrors the universality of the r -process for the lanthanides through the third peak, provided that the abundances of the lighter r -process elements are scaled independently of the heavier ones.

One possible interpretation of this behavior is to associate the weak (or limited) r -process with the lighter r -process elements and the main r -process with the heavier r -process elements. Several theoretical studies have used r -process nucleosynthesis models to explore the transition region between these two sets of elements (e.g., Kratz et al. 2007; Montes et al. 2007; Farouqi et al. 2010; Wanajo 2013; Lorusso et al. 2015; Wu et al. 2016). Kratz et al., for example, found that a weak r -process with neutron densities up to $\log n_n \lesssim 10^{23}$ could produce the lighter elements, including a peak around $A \sim 130$. The r -process reaction network calculations of Lorusso et al., which incorporated newly measured β -decay half-lives of 110 neutron-rich nuclei leading to the second-peak region, indicated that the robust nature of Te production differed from that of the lanthanides. This boundary between the weak and main r -processes likely behaves as a transition, not a cutoff, and some amount of Te and second-peak elements will also be produced by higher neutron densities characteristic of the main r -process.

Despite the multitude of processes that could theoretically produce elements with $A \lesssim 130$, no star in our sample exhibits abundance ratios among Se, Sr through Mo, and Te that are significantly distinct from the others. If multiple r -process sites or other processes contribute to the inventory of lighter r -process elements incorporated into metal-poor stars dating from the early Universe, they must occur relatively infrequently, eject relatively low yields, produce abundance ratios that are not distinct from those listed in Table 2, or some combination of these scenarios. We challenge theorists to identify which r -process sites are capable of producing both the lighter and the heavier r -process elements and producing robust abundance distributions that match the elemental abundance patterns.

Our sample is small and limited by access to high-resolution UV spectra. A few stars in much larger optical-only samples may exhibit deviant $\log \varepsilon(\text{Sr}/\text{Zr})$ or $\log \varepsilon(\text{Y}/\text{Zr})$ ratios (e.g., Lombardo et al. 2022). It will be of interest to evaluate whether such abundance ratios reflect true deviations from the r -process or contributions from another, presumably more rare, process. We challenge observers to expand the sample of stars with high-quality abundance derivations for lighter r -process elements, identify any stars whose lighter r -process element abundance ratios deviate significantly from the

pattern we have characterized, and establish the range of $\log \varepsilon(X/Zr)$ ratios that may occur in metal-poor stars.

5. CONCLUSIONS

We examine the abundances of elements at and between the first and second r -process peaks for eight stars with Se or Te detections. Our data are drawn from the literature, where each study typically focused on one or a few stars at a time. Here, we aggregate these data to characterize the abundance patterns and behaviors of elements from Se through Te for the first time.

The abundances of the lighter r -process elements vary relative to the yields of the heavier r -process elements, but they are not fully decoupled (Figure 1). For this sample of stars, many of the lighter r -process elements, including Se, Sr, Y, Zr, Nb, Mo, and Te exhibit abundance ratios with dispersions ≤ 0.13 dex (26%; Figure 2). This level of consistency matches that of heavier r -process elements. We propose that we have potentially identified a universality analogous to that observed among the lanthanides and third r -process-peak elements, at the precision of available observational data, provided the overall abundances of lighter r -process elements are scaled independently of the heavier ones. The abundance behavior of the elements from Ru through Sn requires further study. We calculate benchmark ratios among the abundances of Se, Sr through Mo, and Te (Table 2). These values reflect yields of events that enriched the gas from which metal-poor stars formed. They can be used to constrain models of candidate sites of r -process nucleosynthesis in the early Universe. We conclude that at least one relatively common r -process source in the early Universe produced a consistent abundance pattern among some light elements spanning the first and second r -process peaks.

ACKNOWLEDGMENTS

We thank J. Lawler and C. Sneden for thoughtful discussions and the referee for helpful suggestions to improve this manuscript. We acknowledge generous support provided by NASA through grants GO-14765, GO-15657, and GO-15951 from the Space Telescope Science Institute, which is operated by the Association of Universities for Research in Astronomy, Incorporated, under NASA contract NAS5-26555. We acknowledge support awarded by the U.S. Na-

tional Science Foundation (NSF): grants PHY 14-30152 (Physics Frontier Center/JINA-CEE), OISE 1927130 (International Research Network for Nuclear Astrophysics/IReNA), AST 1716251 (A.F.), AST 1814512 (E.A.D.H.), and AST 1815403/1815767 (I.U.R.). I.U.R. acknowledges support from the NASA Astrophysics Data Analysis Program, grant 80NSSC21K0627. M.P. acknowledges significant support to NuGrid from STFC (through the University of Hull’s Consolidated Grant ST/R000840/1), and access to VIPER, the University of Hull High Performance Computing Facility. M.P. also acknowledges support from the “Lendület-2014” Programme of the Hungarian Academy of Sciences (Hungary), and from the ERC Consolidator Grant (Hungary) funding scheme (project RADIOSTAR, G.A. n. 724560). M.P. thanks the ChETEC COST Action (CA16117), supported by COST (European Cooperation in Science and Technology), and the ChETEC-INFRA project funded from the European Union’s Horizon 2020 research and innovation programme (grant agreement No 101008324). The work of V.M.P. is supported by NOIR-Lab, which is managed by AURA under a cooperative agreement with the NSF. M.R.M. was supported by the Laboratory Directed Research and Development program of Los Alamos National Laboratory under project number 20200384ER. Los Alamos National Laboratory is operated by Triad National Security, LLC, for the National Nuclear Security Administration of U.S. Department of Energy (Contract No. 89233218CNA000001). R.S. acknowledges support from grant DE-FG02-95-ER40934 awarded by the U.S. Department of Energy. This research has made use of NASA’s Astrophysics Data System Bibliographic Services; the arXiv preprint server operated by Cornell University; the SIMBAD and VizieR databases hosted by the Strasbourg Astronomical Data Center; the ASD hosted by NIST; the Mikulski Archive for Space Telescopes at the Space Telescope Science Institute, which is operated by the Association of Universities for Research in Astronomy, Inc. under NASA contract NAS 5-26555; and the Keck Observatory Archive, which is operated by the W. M. Keck Observatory and the NASA Exoplanet Science Institute, under contract with NASA.

Facility: HST (STIS), Keck (HIRES)

Software: LINEMAKE (Placco et al. 2021), matplotlib (Hunter 2007), MOOG (Sneden 1973; Sobeck et al. 2011), numpy (van der Walt et al. 2011), scipy (Jones et al. 2001)

APPENDIX

Recent advances in laboratory measurements and theoretical calculations of atomic data justify revision of abundances of heavy elements that were published prior to the availability of these data. In the following appendices, we

present revised abundances and, in a few cases, newly derived abundances for a few metal-poor stars with high-quality UV spectra.

A. UPDATED HEAVY-ELEMENT ABUNDANCES IN BD +17°3248

BD +17°3248 has been the subject of many detailed abundance studies over the last two decades. As a result of these many piecemeal reanalyses, the heavy-element abundances for BD +17°3248 are scattered throughout the literature. Different versions of the local thermodynamic equilibrium analysis code MOOG (Sneden 1973) have been used to derive these abundances. Furthermore, new high-quality laboratory atomic data have become available since the original publications. Here, we present a homogeneous, revised set of abundances of 16 r -process elements in BD +17°3248 to make use of these advances.

We use the STIS E230M spectrum of BD +17°3248 ($R = 30,000$, $2280 \leq \lambda \leq 3120 \text{ \AA}$, GO-8342, datasets O5F607010-020, PI Cowan) to rederive abundances for all elements except Ag, for which we use the Keck High Resolution Echelle Spectrometer (HIRES; Vogt et al. 1994) spectrum obtained through the Keck Observatory Archives ($R = 45,000$, $3120 \leq \lambda \leq 4640 \text{ \AA}$; U25H, PI Fuller). All abundances listed in Table A1 are derived with the most recent version of MOOG, which incorporates the treatment of Rayleigh scattering as described in Sobek et al. (2011). We use an ATLAS9 (Castelli & Kurucz 2004) model atmosphere interpolated to the parameters derived by Cowan et al. (2002), effective temperature ($T_{\text{eff}} = 5200 \pm 150 \text{ K}$), log of the surface gravity ($\log g = 1.80 \pm 0.3$), metallicity ($[\text{Fe}/\text{H}] = -2.10 \pm 0.2$), and microturbulence velocity parameter ($v_t = 1.9 \pm 0.2 \text{ km s}^{-1}$). We derive abundances by spectrum synthesis matching using the MOOG “synth” driver, with line lists generated using the LINEMAKE code (Placco et al. 2021). Table A2 lists the recommended abundances. Uncertainties are computed following the method described in Roederer et al. (2018). All other r -process elements not listed in Table A2 should be adopted from the literature, in order of decreasing priority in the case of duplicate values: Sneden et al. (2009), Den Hartog et al. (2005), Roederer et al. (2010), or Cowan et al. (2002).

B. TELLURIUM AND PLATINUM IN HD 19445, HD 84937, AND HD 140283

We use the STIS E230H spectrum of HD 19445 ($R = 114,000$, $1879 \leq \lambda \leq 2150 \text{ \AA}$, GO-14672, datasets OD65A1010-A8030, PI Peterson) to derive its Te abundance and an upper limit on Pt. We adopt the model atmosphere derived by Peterson et al. (2020), $T_{\text{eff}} = 6070 \text{ K}$, $\log g = 4.4$, $[\text{Fe}/\text{H}] = -2.15$, and $v_t = 1.3 \text{ km s}^{-1}$. We derive abundances by spectrum synthesis matching using the MOOG “synth” driver, with line lists generated using LINEMAKE. All atomic data for these lines are identical to the data adopted by Roederer et al. (2022). We detect one Te I line, $\lambda 2142$, which yields $\log \varepsilon(\text{Te}) = 0.65 \pm 0.15$, or $[\text{Te}/\text{Fe}] = +0.62 \pm 0.15$. No Pt I lines are detected in this spectrum. One of the strongest ones, at $\lambda 2659$, yields an upper limit $\log \varepsilon(\text{Pt}) < +0.20$, or $[\text{Pt}/\text{Fe}] < +0.73$.

We use the STIS E230H spectrum of HD 84937 ($R = 114,000$, $2128 \leq \lambda \leq 3143 \text{ \AA}$, GO-14161, datasets OCTKA6010-D020, PI Peterson) to derive its Te abundance and an upper limit on Pt. We adopt the model atmosphere derived by Peterson et al. (2020), $T_{\text{eff}} = 6300 \text{ K}$, $\log g = 4.0$, $[\text{Fe}/\text{H}] = -2.25$, and $v_t = 1.3 \text{ km s}^{-1}$. We detect two Te I lines, $\lambda 2142$ and $\lambda 2385$, which yield $\log \varepsilon(\text{Te})$ abundances of 0.29 ± 0.10 and 0.44 ± 0.20 , respectively. The mean Te abundance is $\log \varepsilon(\text{Te}) = 0.33 \pm 0.11$, or $[\text{Te}/\text{Fe}] = +0.40 \pm 0.15$. No Pt I lines are detected in this spectrum. The Pt I line at 2659 \AA yields an upper limit $\log \varepsilon(\text{Pt}) < -0.10$, or $[\text{Pt}/\text{Fe}] < +0.53$.

We use two STIS E230H spectra ($R = 114,000$, $1932 \leq \lambda \leq 2212 \text{ \AA}$, GO-7348, datasets O55Z01030-01050, PI Edvardsson; $R = 50,000$, $2390 \leq \lambda \leq 3140 \text{ \AA}$, GO-9455, datasets O6LM71010-40, PI Peterson) to derive upper limits on Te and Pt in HD 140283. We adopt the model atmosphere derived by Roederer (2012), $T_{\text{eff}} = 5600 \text{ K}$, $\log g = 3.66$, $[\text{Fe}/\text{H}] = -2.62$, and $v_t = 1.15 \text{ km s}^{-1}$. The Te I line at 2142 \AA appears to be broadened by an Fe I line, so we use the Te I line at 2259 \AA to derive $\log \varepsilon(\text{Te}) < 0.20$, or $[\text{Te}/\text{Fe}] < +0.59$. The Pt I line at 2659 \AA yields an upper limit $\log \varepsilon(\text{Pt}) < -1.40$, or $[\text{Pt}/\text{Fe}] < -0.45$.

C. LUTETIUM AND HAFNIUM IN HD 108317 AND HD 128279

New atomic data motivate a reanalysis of the lutetium (Lu, $Z = 71$) and hafnium (Hf, $Z = 72$) abundances in HD 108317 and HD 128279. Den Hartog et al. (2020) measured the hyperfine splitting constants for 16 levels of ionized ^{175}Lu , the dominant Lu isotope, and presented new line component patterns for 35 Lu II transitions. Furthermore, we identify a moderately strong line at the wavelength of the Lu II line at 2615.41 \AA in several stars with low levels of heavy r -process elements (see, e.g., the observational material listed in table 3 of Roederer & Lawler 2021). This line yields high Lu abundances, $\log \varepsilon(\text{Lu}/\text{Eu}) \gtrsim 0.5$. Such high ratios are not likely, and they disagree with $\log \varepsilon(\text{Lu}/\text{Eu})$ ratios (≈ -0.4) derived from other Lu II lines in the highly r -process-enhanced star HD 222925 (Roederer et al. 2022). We conclude that some of the absorption at this wavelength is not due to Lu II, at least in stars without high levels of r -process enhancement, such as HD 222925. We revise the Lu abundances in HD 108317 and HD 128279 to be upper limits: $\log \varepsilon(\text{Lu}) < -1.64$ and < -1.92 , respectively.

Den Hartog et al. (2021) measured the branching fractions for 199 transitions of ionized Hf and presented new $\log(gf)$ values calculated from these measurements. We do not detect Hf II lines at 2322.48 , 2861.70 , or 3012.90 \AA in either

Table A1. Updated Abundances from UV Spectrum of BD +17°3248

Species	λ (Å)	E_{low} (eV)	$\log(gf)$	Ref.	$\log \epsilon$	Fit Unc. [dex]	Supersedes
Ge I	2651.17	0.17	-0.07	1	0.62	0.20	...
Ge I	2691.34	0.07	-0.81	1	0.42	0.20	...
Ge I	3039.07	0.88	-0.07	1	0.47	0.15	15
As I	2288.11	1.35	-0.06	2	< -0.10
Nb II	2910.59	0.38	-0.16	3	-0.21	0.15	...
Nb II	2911.74	0.33	-0.28	3	-0.18	0.20	...
Mo II	2660.58	1.49	-0.14	4	0.18	0.15	...
Mo II	2871.51	1.54	+0.06	4	0.00	0.15	...
Mo II	2911.92	1.60	-0.10	4	0.30	0.15	...
Mo II	2930.50	1.49	-0.23	4	0.09	0.15	...
Ag I	3280.68	0.00	-0.02	5	-0.86	0.20	8
Ag I	3382.89	0.00	-0.33	5	-0.62	0.15	8
Cd I	2288.02	0.00	+0.15	6	-0.99	0.15	8
In II	2306.06	0.00	-2.30	2	< -0.10
Te I	2385.79	0.59	-0.81	7	0.42	0.30	7
Lu II	2615.41	0.00	+0.11	8	< -1.47	...	8
Lu II	2911.39	1.76	+0.45	9	-1.33	0.20	...
Hf II	2322.48	0.00	-1.14	10	-1.10	0.20	...
Hf II	2641.41	1.04	+0.57	11	-0.67	0.15	...
Hf II	2861.70	0.45	-0.32	10	-1.14	0.20	...
Hf II	3012.90	0.00	-0.61	11	-0.82	0.20	...
Os I	3058.65	0.00	-0.41	12	0.06	0.20	15
Os II	2282.28	0.00	-0.14	13	-0.39	0.15	8
Ir I	2639.71	0.00	-0.31	14	-0.11	0.15	...
Ir I	2924.79	0.00	-0.66	2	0.22	0.25	...
Au I	2675.94	0.00	-0.60	2	-0.60	0.30	16

References—1 = Li et al. (1999); 2 = Roederer et al. (2022); 3 = Nilsson & Ivarsson (2008); 4 = Sikström et al. (2001); 5 = Hansen et al. (2012); 6 = Morton (2000); 7 = Roederer et al. (2012a); 8 = Roederer et al. (2010); 9 = Den Hartog et al. (2020); 10 = Den Hartog et al. (2021); 11 = Lawler et al. (2007); 12 = Quinet et al. (2006); 13 = Ivarsson et al. (2004); 14 = NIST (Kramida et al. 2021); 15 = Cowan et al. (2005); 16 = Cowan et al. (2002).

star. The upper limits derived from these lines are lower than the Hf abundances derived previously from the Hf II lines at 2641.41 or 4093.15 Å (Roederer et al. 2012b), so we conclude that the previous results included unidentified blends. We recommend $\log \epsilon(\text{Hf}) < -1.40$ and $\log \epsilon(\text{Hf}) < -1.70$ (both from the $\lambda 2322$ line) in HD 108317 and HD 128279, respectively.

D. THE COMPLETE HEAVY-ELEMENT ABUNDANCE PATTERNS

Table D3 lists the heavy-element abundance patterns shown in Figure 2. It also includes the stellar parameters adopted by previous studies. Any future study that makes use of these data should cite the original references, which are listed in Table 1.

Table A2. Updated Mean Abundances in BD +17°3248

Element	$\log \epsilon_{\odot}^a$	$\log \epsilon$	$[X/Fe]^b$	Unc.	N_{lines}	Notes
				[dex]		
Ge	3.65	0.50	-1.05	0.15	3	...
As	2.30	< -0.10	< -0.30	...	1	...
Sr	2.87	1.09	+0.32	0.10	2	<i>c</i>
Y	2.21	0.00	-0.11	0.05	11	<i>d</i>
Zr	2.58	0.83	+0.35	0.14	19	<i>e</i>
Nb	1.46	-0.22	+0.42	0.20	3	<i>f</i>
Mo	1.88	0.14	+0.36	0.10	5	<i>f</i>
Ag	0.94	-0.71	+0.45	0.15	2	<i>g</i>
Cd	1.71	-0.99	-0.60	0.16	1	...
In	0.80	< -0.10	< +1.20	...	1	...
Te	2.18	0.42	+0.34	0.30	1	...
Lu	0.10	-1.33	+0.67	0.20	1	<i>h</i>
Hf	0.85	-0.66	+0.59	0.23	10	<i>i</i>
Os	1.40	-0.11	+0.59	0.16	3	<i>j</i>
Ir	1.38	0.15	+0.87	0.15	5	<i>k</i>
Au	0.92	-0.60	+0.58	0.30	1	...

^aAsplund et al. (2009)

^bReferenced to $[\text{Fe}/\text{H}] = -2.10$

^cAbundance from Cowan et al. (2002) corrected to the $\log(gf)$ scale of the NIST ASD (Kramida et al. 2021)

^dAbundance from Cowan et al. (2002) corrected to the $\log(gf)$ scale of Biémont et al. (2011)

^eAbundance from Cowan et al. (2002) corrected to the $\log(gf)$ scale of Ljung et al. (2006)

^fMean abundance includes one line from Roederer et al. (2010)

^gAbundance from Roederer et al. (2010) corrected to the $\log(gf)$ scale of Hansen et al. (2012), including hyperfine splitting structure and isotope shifts

^hSee Appendix C

ⁱMean abundance includes six lines from Lawler et al. (2007)

^jMean abundance includes one line from Cowan et al. (2005)

^kMean abundance includes three lines from Cowan et al. (2005)

REFERENCES

- Abohalima, A., & Frebel, A. 2018, ApJS, 238, 36
- Aoki, M., Ishimaru, Y., Aoki, W., & Wanajo, S. 2017, ApJ, 837, 8
- Aoki, W., Beers, T. C., Honda, S., & Carollo, D. 2010, ApJL, 723, L201
- Aoki, W., Honda, S., Beers, T. C., et al. 2005, ApJ, 632, 611
- Arcones, A., & Montes, F. 2011, ApJ, 731, 5
- Arcones, A., & Thielemann, F. K. 2013, Journal of Physics G Nuclear Physics, 40, 013201

Table D3. Stellar Parameters and Heavy-Element Abundance Patterns for the Sun and Eight Stars in the Sample

Parameter	Sun	HD 222925	BD +17°3248	HD 108317	HD 160617	HD 84937	HD 19445	HD 128279	HD 140283
or abundance									
T_{eff} (K)	...	5636	5200	5100	5950	6300	6070	5080	5750
$\log g$...	2.54	1.80	2.67	3.90	4.00	4.40	2.57	3.70
v_t (km s ⁻¹)	...	2.20	1.90	1.50	1.30	1.30	1.30	1.60	1.40
[Fe/H]	...	-1.46	-2.10	-2.37	-1.77	-2.25	-2.15	-2.46	-2.57
$\log \varepsilon(\text{Se})$	3.34	2.62	...	1.28	1.56	1.23	1.56	0.55	0.65
$\log \varepsilon(\text{Sr})$	2.87	1.98	1.09	0.48	1.22	1.04	1.00	-0.18	0.07
$\log \varepsilon(\text{Y})$	2.21	1.04	0.00	-0.42	0.25	-0.03	0.13	-0.89	-0.77
$\log \varepsilon(\text{Zr})$	2.58	1.74	0.83	0.45	1.05	0.65	0.82	0.00	-0.05
$\log \varepsilon(\text{Nb})$	1.46	0.71	-0.22	-0.86	-0.88	...
$\log \varepsilon(\text{Mo})$	1.88	1.36	0.14	-0.05	0.61	0.39	0.48	-0.56	-0.44
$\log \varepsilon(\text{Ru})$	1.75	1.32	0.34	-0.04	0.59	0.47	0.44	-0.63	...
$\log \varepsilon(\text{Rh})$	0.91	0.64	-0.57	-0.84
$\log \varepsilon(\text{Pd})$	1.57	1.05	-0.05	-0.67	-0.07	-1.24	...
$\log \varepsilon(\text{Ag})$	0.94	0.44	-0.71	-1.34	-0.89
$\log \varepsilon(\text{Cd})$	1.71	0.34	-0.99	-1.15	-0.03	-0.17	-0.37	-1.32	-1.34
$\log \varepsilon(\text{In})$	0.80	0.51	< -0.10
$\log \varepsilon(\text{Sn})$	2.04	1.39	0.38	-0.44	0.11	...	-1.06
$\log \varepsilon(\text{Sb})$	1.01	0.37
$\log \varepsilon(\text{Te})$	2.18	1.63	0.42	0.06	0.67	0.33	0.65	-0.12	<0.20
$\log \varepsilon(\text{Ba})$	2.18	1.26	0.48	-0.32	0.44	-0.23	0.00	-1.03	-1.09
$\log \varepsilon(\text{La})$	1.10	0.51	-0.42	-1.12	-0.36	-1.64	...
$\log \varepsilon(\text{Ce})$	1.58	0.85	-0.11	-0.68	0.06	-1.15	...
$\log \varepsilon(\text{Pr})$	0.72	0.22	-0.71	-0.90
$\log \varepsilon(\text{Nd})$	1.42	0.88	-0.09	-0.71	-0.03	-1.23	...
$\log \varepsilon(\text{Sm})$	0.96	0.62	-0.34	-1.05	-0.45	-1.50	...
$\log \varepsilon(\text{Eu})$	0.52	0.38	-0.68	-1.37	-0.81	-1.35	-1.26	-1.96	-2.27
$\log \varepsilon(\text{Gd})$	1.07	0.82	-0.14	-0.82	-0.30
$\log \varepsilon(\text{Tb})$	0.30	0.18	-0.91	-1.30
$\log \varepsilon(\text{Dy})$	1.10	1.01	-0.04	-0.75	-0.20	-1.35	...
$\log \varepsilon(\text{Ho})$	0.48	0.12	-0.70	-1.50	-1.71	...
$\log \varepsilon(\text{Er})$	0.92	0.73	-0.25	-0.94	-0.35	-1.54	...
$\log \varepsilon(\text{Tm})$	0.10	-0.09	-1.12	-1.80	-2.24	...
$\log \varepsilon(\text{Yb})$	0.84	0.55	-0.27	-1.13	-0.42	-1.69	...
$\log \varepsilon(\text{Lu})$	0.10	-0.04	-1.33	< -1.64	< -1.92	...
$\log \varepsilon(\text{Hf})$	0.85	0.32	-0.66	< -1.40	< -1.70	...
$\log \varepsilon(\text{W})$	0.85	0.02
$\log \varepsilon(\text{Re})$	0.26	0.16
$\log \varepsilon(\text{Os})$	1.40	1.17	-0.11	-0.69	-0.12
$\log \varepsilon(\text{Ir})$	1.38	1.28	0.15
$\log \varepsilon(\text{Pt})$	1.62	1.45	0.53	-0.40	0.44	< -0.10	<0.20	...	< -1.40
$\log \varepsilon(\text{Au})$	0.92	0.53	-0.60	-1.64

- Asplund, M., Grevesse, N., Sauval, A. J., & Scott, P. 2009, *ARA&A*, 47, 481
- Banerjee, P., Qian, Y.-Z., & Heger, A. 2018, *ApJ*, 865, 120
- Barbuy, B., Spite, M., Hill, V., et al. 2011, *A&A*, 534, A60
- Barklem, P. S., Christlieb, N., Beers, T. C., et al. 2005, *A&A*, 439, 129
- Barnes, J., Zhu, Y. L., Lund, K. A., et al. 2021, *ApJ*, 918, 44
- Bertolli, M. G., Herwig, F., Pignatari, M., & Kawano, T. 2013, arXiv e-prints, arXiv:1310.4578.
<https://arxiv.org/abs/1310.4578>
- Biéumont, É., Blagoev, K., Engström, L., et al. 2011, *MNRAS*, 414, 3350
- Bisterzo, S., Gallino, R., Straniero, O., Cristallo, S., & Käppeler, F. 2011, *MNRAS*, 418, 284
- Bisterzo, S., Travaglio, C., Gallino, R., Wiescher, M., & Käppeler, F. 2014, *ApJ*, 787, 10
- Bisterzo, S., Travaglio, C., Wiescher, M., Käppeler, F., & Gallino, R. 2017, *ApJ*, 835, 97
- Burris, D. L., Pilachowski, C. A., Armandroff, T. E., et al. 2000, *ApJ*, 544, 302
- Cain, M., Frebel, A., Gull, M., et al. 2018, *ApJ*, 864, 43
- Castelli, F., & Kurucz, R. L. 2004, ArXiv e-prints.
<https://arxiv.org/abs/astro-ph/0405087>
- Cescutti, G., Chiappini, C., Hirschi, R., Meynet, G., & Frischknecht, U. 2013, *A&A*, 553, A51
- Choplin, A., Hirschi, R., Meynet, G., et al. 2018, *A&A*, 618, A133
- Clarkson, O., Herwig, F., & Pignatari, M. 2018, *MNRAS*, 474, L37
- Côté, B., Denissenkov, P., Herwig, F., et al. 2018, *ApJ*, 854, 105
- Côté, B., Eichler, M., Arcones, A., et al. 2019, *ApJ*, 875, 106
- Cowan, J. J., Sneden, C., Lawler, J. E., et al. 2021, *Reviews of Modern Physics*, 93, 015002
- Cowan, J. J., Sneden, C., Truran, J. W., & Burris, D. L. 1996, *ApJL*, 460, L115
- Cowan, J. J., Sneden, C., Burles, S., et al. 2002, *ApJ*, 572, 861
- Cowan, J. J., Sneden, C., Beers, T. C., et al. 2005, *ApJ*, 627, 238
- Den Hartog, E. A., Herd, M. T., Lawler, J. E., et al. 2005, *ApJ*, 619, 639
- Den Hartog, E. A., Lawler, J. E., & Roederer, I. U. 2020, *ApJS*, 248, 10
- . 2021, *ApJS*, 254, 5
- Dillmann, I., Kratz, K. L., Wöhr, A., et al. 2003, *PhRvL*, 91, 162503
- Drout, M. R., Piro, A. L., Shappee, B. J., et al. 2017, *Science*, 358, 1570
- Eichler, M., Arcones, A., Kelic, A., et al. 2015, *ApJ*, 808, 30
- Farouqi, K., Kratz, K. L., Pfeiffer, B., et al. 2010, *ApJ*, 712, 1359
- Farouqi, K., Thielemann, F. K., Rosswog, S., & Kratz, K. L. 2022, *A&A*, 663, A70
- Fernández, R., Foucart, F., & Lippuner, J. 2020, *MNRAS*, 497, 3221
- Fischer, T., Whitehouse, S. C., Mezzacappa, A., Thielemann, F. K., & Liebendörfer, M. 2010, *A&A*, 517, A80
- Fischer, T., Wu, M.-R., Wehmeyer, B., et al. 2020, *ApJ*, 894, 9
- Fontes, C. J., Fryer, C. L., Hungerford, A. L., Wollaeger, R. T., & Korobkin, O. 2020, *MNRAS*, 493, 4143
- François, P., Depagne, E., Hill, V., et al. 2007, *A&A*, 476, 935
- Frebel, A. 2018, *Annual Review of Nuclear and Particle Science*, 68, 237
- Frebel, A., Simon, J. D., Geha, M., & Willman, B. 2010, *ApJ*, 708, 560
- Frischknecht, U., Hirschi, R., Pignatari, M., et al. 2016, *MNRAS*, 456, 1803
- Fröhlich, C., Martínez-Pinedo, G., Liebendörfer, M., et al. 2006, *PhRvL*, 96, 142502
- Fulbright, J. P. 2000, *AJ*, 120, 1841
- Goriely, S. 1999, *A&A*, 342, 881
- Grossman, D., Korobkin, O., Rosswog, S., & Piran, T. 2014, *MNRAS*, 439, 757
- Hansen, C. J., Andersen, A. C., & Christlieb, N. 2014, *A&A*, 568, A47
- Hansen, C. J., & Primas, F. 2011, *A&A*, 525, L5
- Hansen, C. J., Primas, F., Hartman, H., et al. 2012, *A&A*, 545, A31
- Hansen, T. T., Simon, J. D., Marshall, J. L., et al. 2017, *ApJ*, 838, 44
- Hayek, W., Wiesendahl, U., Christlieb, N., et al. 2009, *A&A*, 504, 511
- Herwig, F., Woodward, P. R., Lin, P.-H., Knox, M., & Fryer, C. 2014, *ApJL*, 792, L3
- Hirschi, R., Meynet, G., & Maeder, A. 2004, *A&A*, 425, 649
- Holmbeck, E. M., Beers, T. C., Roederer, I. U., et al. 2018, *ApJL*, 859, L24
- Holmbeck, E. M., Hansen, T. T., Beers, T. C., et al. 2020, *ApJS*, 249, 30
- Honda, S., Aoki, W., Ishimaru, Y., & Wanajo, S. 2007, *ApJ*, 666, 1189
- Honda, S., Aoki, W., Ishimaru, Y., Wanajo, S., & Ryan, S. G. 2006, *ApJ*, 643, 1180

- Honda, S., Aoki, W., Kajino, T., et al. 2004, *ApJ*, 607, 474
- Hotokezaka, K., Piran, T., & Paul, M. 2015, *Nature Physics*, 11, 1042
- Hunter, J. D. 2007, *Computing in Science and Engineering*, 9, 90
- Ishigaki, M. N., Aoki, W., & Chiba, M. 2013, *ApJ*, 771, 67
- Ivans, I. I., Simmerer, J., Sneden, C., et al. 2006, *ApJ*, 645, 613
- Ivarsson, S., Wahlgren, G. M., Dai, Z., Lundberg, H., & Leckrone, D. S. 2004, *A&A*, 425, 353
- Ji, A. P., Frebel, A., Chiti, A., & Simon, J. D. 2016, *Nature*, 531, 610
- Ji, A. P., Simon, J. D., Frebel, A., Venn, K. A., & Hansen, T. T. 2019, *ApJ*, 870, 83
- Johnson, J. A. 2002, *ApJS*, 139, 219
- Johnson, J. A., & Bolte, M. 2002, *ApJ*, 579, 616
- Jones, E., Oliphant, T., Peterson, P., & et al. 2001, *SciPy: Open source scientific tools for Python*, online. <http://www.scipy.org/>
- Kasen, D., Badnell, N. R., & Barnes, J. 2013, *ApJ*, 774, 25
- Kimble, R. A., Woodgate, B. E., Bowers, C. W., et al. 1998, *ApJL*, 492, L83
- Kramida, A., Ralchenko, Y., Reader, J., & NIST ASD Team. 2021, NIST Atomic Spectra Database (ver. 5.9), [Online]. Available: <https://physics.nist.gov/asd>, National Institute of Standards and Technology, Gaithersburg, MD.
- Kratz, K.-L., Bitouzet, J.-P., Thielemann, F.-K., Moeller, P., & Pfeiffer, B. 1993, *ApJ*, 403, 216
- Kratz, K.-L., Farouqi, K., Pfeiffer, B., et al. 2007, *ApJ*, 662, 39
- Lai, D. K., Bolte, M., Johnson, J. A., et al. 2008, *ApJ*, 681, 1524
- Lawler, J. E., den Hartog, E. A., Labby, Z. E., et al. 2007, *ApJS*, 169, 120
- Li, Z. S., Norin, J., Persson, A., et al. 1999, *PhRvA*, 60, 198
- Limongi, M., & Chieffi, A. 2018, *ApJS*, 237, 13
- Ljung, G., Nilsson, H., Asplund, M., & Johansson, S. 2006, *A&A*, 456, 1181
- Lombardo, L., Bonifacio, P., François, P., et al. 2022, *A&A*, 665, A10
- Lorusso, G., Nishimura, S., Xu, Z. Y., et al. 2015, *PhRvL*, 114, 192501
- Mashonkina, L., Christlieb, N., Barklem, P. S., et al. 2010, *A&A*, 516, A46
- Mashonkina, L., Christlieb, N., & Eriksson, K. 2014, *A&A*, 569, A43
- McWilliam, A. 1998, *AJ*, 115, 1640
- Montes, F., Beers, T. C., Cowan, J., et al. 2007, *ApJ*, 671, 1685
- Morton, D. C. 2000, *ApJS*, 130, 403
- Nilsson, H., & Ivarsson, S. 2008, *A&A*, 492, 609
- Nishimura, N., Hirschi, R., Rauscher, T., St. J. Murphy, A., & Cescutti, G. 2017, *MNRAS*, 469, 1752
- Nishimura, N., Takiwaki, T., & Thielemann, F.-K. 2015, *ApJ*, 810, 109
- Panov, I. V., Korneev, I. Y., & Thielemann, F.-K. 2008, *Astronomy Letters*, 34, 189
- Peterson, R. C., Barbuy, B., & Spite, M. 2020, *A&A*, 638, A64
- Pian, E., D’Avanzo, P., Benetti, S., et al. 2017, *Nature*, 551, 67
- Pignatari, M., Gallino, R., Heil, M., et al. 2010, *ApJ*, 710, 1557
- Pignatari, M., Gallino, R., Meynet, G., et al. 2008, *ApJL*, 687, L95
- Pignatari, M., & Herwig, F. 2012, *Nuclear Physics News*, 22, 18
- Pignatari, M., Hirschi, R., Wiescher, M., et al. 2013, *ApJ*, 762, 31
- Placco, V. M., Sneden, C., Roederer, I. U., et al. 2021, *Research Notes of the American Astronomical Society*, 5, 92
- Prantzos, N., Abia, C., Cristallo, S., Limongi, M., & Chieffi, A. 2020, *MNRAS*, 491, 1832
- Preston, G. W., Sneden, C., Thompson, I. B., Sheckman, S. A., & Burley, G. S. 2006, *AJ*, 132, 85
- Qian, Y. Z., & Wasserburg, G. J. 2008, *ApJ*, 687, 272
- Quinet, P., Palmeri, P., Biéumont, É., et al. 2006, *A&A*, 448, 1207
- Reiter, M. P., Ayet San Andrés, S., Nikas, S., et al. 2020, *PhRvC*, 101, 025803
- Roberts, L. F., Woosley, S. E., & Hoffman, R. D. 2010, *ApJ*, 722, 954
- Roederer, I. U. 2012, *ApJ*, 756, 36
- Roederer, I. U., Cowan, J. J., Preston, G. W., et al. 2014a, *MNRAS*, 445, 2970
- Roederer, I. U., Karakas, A. I., Pignatari, M., & Herwig, F. 2016a, *ApJ*, 821, 37
- Roederer, I. U., & Lawler, J. E. 2012, *ApJ*, 750, 76
- . 2021, *ApJ*, 912, 119
- Roederer, I. U., Preston, G. W., Thompson, I. B., et al. 2014b, *AJ*, 147, 136
- Roederer, I. U., Sakari, C. M., Placco, V. M., et al. 2018, *ApJ*, 865, 129
- Roederer, I. U., Sneden, C., Lawler, J. E., & Cowan, J. J. 2010, *ApJL*, 714, L123
- Roederer, I. U., Lawler, J. E., Cowan, J. J., et al. 2012a, *ApJL*, 747, L8

- Roederer, I. U., Lawler, J. E., Sobek, J. S., et al. 2012b, *ApJS*, 203, 27
- Roederer, I. U., Schatz, H., Lawler, J. E., et al. 2014c, *ApJ*, 791, 32
- Roederer, I. U., Mateo, M., Bailey, III, J. I., et al. 2016b, *AJ*, 151, 82
- Roederer, I. U., Lawler, J. E., Den Hartog, E. A., et al. 2022, *ApJS*, 260, 27
- Rosswog, S., Korobkin, O., Arcones, A., Thielemann, F. K., & Piran, T. 2014, *MNRAS*, 439, 744
- Shibagaki, S., Kajino, T., Mathews, G. J., et al. 2016, *ApJ*, 816, 79
- Siegel, D. M., Barnes, J., & Metzger, B. D. 2019, *Nature*, 569, 241
- Sikström, C. M., Pihlemark, H., Nilsson, H., et al. 2001, *Journal of Physics B Atomic Molecular Physics*, 34, 477
- Siqueira Mello, C., Spite, M., Barbuy, B., et al. 2013, *A&A*, 550, A122
- Siqueira Mello, C., Hill, V., Barbuy, B., et al. 2014, *A&A*, 565, A93
- Skúladóttir, Á., & Salvadori, S. 2020, *A&A*, 634, L2
- Sneden, C., Cowan, J. J., Burris, D. L., & Truran, J. W. 1998, *ApJ*, 496, 235
- Sneden, C., Cowan, J. J., & Gallino, R. 2008, *ARA&A*, 46, 241
- Sneden, C., Lawler, J. E., Cowan, J. J., Ivans, I. I., & Den Hartog, E. A. 2009, *ApJS*, 182, 80
- Sneden, C., Cowan, J. J., Lawler, J. E., et al. 2003, *ApJ*, 591, 936
- Sneden, C. A. 1973, PhD thesis, The University of Texas at Austin.
- Sobek, J. S., Kraft, R. P., Sneden, C., et al. 2011, *AJ*, 141, 175
- Spite, F., Spite, M., Barbuy, B., et al. 2018, *A&A*, 611, A30
- Tanvir, N. R., Levan, A. J., González-Fernández, C., et al. 2017, *ApJL*, 848, L27
- Thielemann, F.-K., Eichler, M., Panov, I. V., & Wehmeyer, B. 2017, *Annual Review of Nuclear and Particle Science*, 67, 253
- Travaglio, C., Gallino, R., Arnone, E., et al. 2004, *ApJ*, 601, 864
- van der Walt, S., Colbert, S. C., & Varoquaux, G. 2011, *Computing in Science Engineering*, 13, 22
- Vassh, N., Mumpower, M. R., McLaughlin, G. C., Sprouse, T. M., & Surman, R. 2020, *ApJ*, 896, 28
- Vogt, S. S., Allen, S. L., Bigelow, B. C., et al. 1994, in *Proc. SPIE*, Vol. 2198, *Instrumentation in Astronomy VIII*, ed. D. L. Crawford & E. R. Craine, 362
- Wallner, A., Faestermann, T., Feige, J., et al. 2015, *Nature Communications*, 6, 5956
- Wallner, A., Froehlich, M. B., Hotchkis, M. A. C., et al. 2021, *Science*, 372, 742
- Wanajo, S. 2013, *ApJL*, 770, L22
- Wanajo, S., Müller, B., Janka, H.-T., & Heger, A. 2018, *ApJ*, 852, 40
- Wasserburg, G. J., Busso, M., & Gallino, R. 1996, *ApJL*, 466, L109
- Watson, D., Hansen, C. J., Selsing, J., et al. 2019, *Nature*, 574, 497
- Wehmeyer, B., Fröhlich, C., Côté, B., Pignatari, M., & Thielemann, F. K. 2019, *MNRAS*, 487, 1745
- Westin, J., Sneden, C., Gustafsson, B., & Cowan, J. J. 2000, *ApJ*, 530, 783
- Winteler, C., Käppeli, R., Perego, A., et al. 2012, *ApJL*, 750, L22
- Woodgate, B. E., Kimble, R. A., Bowers, C. W., et al. 1998, *PASP*, 110, 1183
- Woodward, P. R., Herwig, F., & Lin, P.-H. 2015, *ApJ*, 798, 49
- Wu, M.-R., Barnes, J., Martínez-Pinedo, G., & Metzger, B. D. 2019, *PhRvL*, 122, 062701
- Wu, M.-R., Fernández, R., Martínez-Pinedo, G., & Metzger, B. D. 2016, *MNRAS*, 463, 2323
- Wu, X., Wang, L., Shi, J., Zhao, G., & Grupp, F. 2015, *A&A*, 579, A8
- Yong, D., Kobayashi, C., Da Costa, G. S., et al. 2021, *Nature*, 595, 223
- Zhu, Y., Wollaeger, R. T., Vassh, N., et al. 2018, *ApJL*, 863, L23
- Zhu, Y. L., Lund, K. A., Barnes, J., et al. 2021, *ApJ*, 906, 94